Modulating the Photoluminescence of Bridged Silsesquioxanes Incorporating Eu^{3+}-Complexed n,n'-Diureido-2,2'-bipyridine Isomers: Application for Luminescent Solar Concentrators
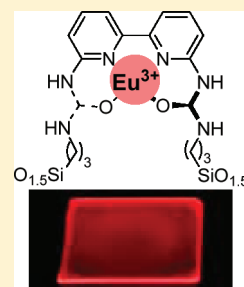
Julien Graffion,[†,‡] Xavier Cattoën,[†] Michel Wong Chi Man,*[,†] Vasco R. Fernandes,[‡,§] Paulo S. André,[§] Rute A. S. Ferreira,[‡] and Luís D. Carlos*[,‡]

[†]Institut Charles Gerhardt Montpellier, 8, Rue de l'École Normale, 34296 Montpellier, France

[‡]Department of Physics and CICECO, and [§]Instituto de Telecomunicações and Department of Physics, Universidade de Aveiro, 3810-193 Aveiro, Portugal

Ⓢ Supporting Information

ABSTRACT: Two new urea-bipyridine derived bridged organosilanes (**P5** and **P6**) have been synthesized and their hydrolysis—condensation under nucleophilic catalysis in the presence of Eu^{3+} salts led to luminescent bridged silsesquioxanes (**M5-Eu** and **M6-Eu**). An important loading of Eu^{3+} (up to 11%$_w$) can be obtained for the material based on the 6,6'-isomer. Indeed the photoluminescence properties of these materials, that have been investigated in depth (photoluminescence (PL), quantum yield, lifetimes), show a significantly different complexation mode of the Eu^{3+} ions for **M6-Eu**, compared with **M4-Eu** (obtained from the already-reported 4,4'-isomer) and **M5-Eu**. Moreover, **M6-Eu** exhibits the highest absolute emission quantum yield value (0.18 ± 0.02) among these three materials. The modification of the sol composition upon the addition of a malonamide derivative led to similar luminescent features but with an increased quantum yield (0.26 ± 0.03). In addition, **M6-Eu** can be processed as thin films by spin-coating on glass substrates, leading to plates coated by a thin layer (∼54 nm) of Eu^{3+}-containing hybrid silica exhibiting one of the highest emission quantum yields reported so far for films of Eu^{3+}-containing hybrids (0.34 ± 0.03) and an interesting potential as new luminescent solar concentrators (LSCs) with an optical conversion efficiency of ∼4%. The ratio between the light guided to the film edges and the one emitted by the surface of the film was quantified through the mapping of the intensity of the red pixels (in the RGB color model) from a film image. This quantification enabled a more accurate estimation of the transport losses due to the scattering of the emitted light in the film (0.40), thereby correcting the initial optical conversion efficiency to a value of 1.7%.

KEYWORDS: bridged silsesquioxane, luminescent solar concentrators, sol—gel, photoluminescence, thin films

1. INTRODUCTION

Research on organic—inorganic hybrid materials containing trivalent lanthanide ions (Ln^{3+}) is a very active field that has rapidly shifted in the last couple of years to the development of eco-friendly, versatile, and multifunctional systems with applications spanning domains as diverse as optics, environment, energy, and biomedicine.[1−4]

Particularly, highly efficient blue-, green-, and red-emitting Ln^{3+}-containing organic—inorganic hybrid phosphors are of widespread interest in materials science, because of their important role in displays, lighting technologies, and solar energy conversion. The processability of the hybrid materials impacts significantly on the integration, miniaturization, and multifunctionalisation of devices and presently the focus is placed on large-scale thin film technology, namely in the hybrid/substrate and multilayers adhesion, thickness and homogeneity control, low surface roughness, and optical transparency.

Transparent thin films of Ln^{3+}-based hybrids find widespread applicability in disparate contexts, spanning domains such as agriculture and horticulture,[2] active coatings for improving the conversion efficiency of Si-based solar cells,[5,6] and for luminescent solar concentrators (LSCs).[7−10] LSCs make use of a transparent substrate doped with fluorophores, such as organic dyes, quantum dots (QDs), or Ln^{3+} complexes, that successfully convert the ultraviolet (UV) component of sunlight into visible light. Through total internal reflection, a large fraction of the emitted light (theoretically ∼75%—80% for a phosphor layer with a refractive index of 1.51[11]) is trapped within the plate and guided to the edges, where it emerges in a concentrated form that can be collected by solar cells.[10−14] Connection of the coated LSCs with monocrystalline silicon (c-Si) solar cells resulted in photovoltaic outputs 10%—15% higher than those observed in systems using the bare LSC plates.[4] The Ln^{3+} complexes exhibit insignificant reabsorption effects (nonoverlap between absorption and emission), relatively to those typical of organic dyes and QDs, which is an important advantage for LSC technology. However, the number of papers involved with LSCs incorporating Ln^{3+} complexes is very scarce.[8−10]

Thermally and chemically stable transparent thin films of hierarchically organized Ln^{3+}-containing organic—inorganic hybrids were amply reported in the past decade. For instance, full-color
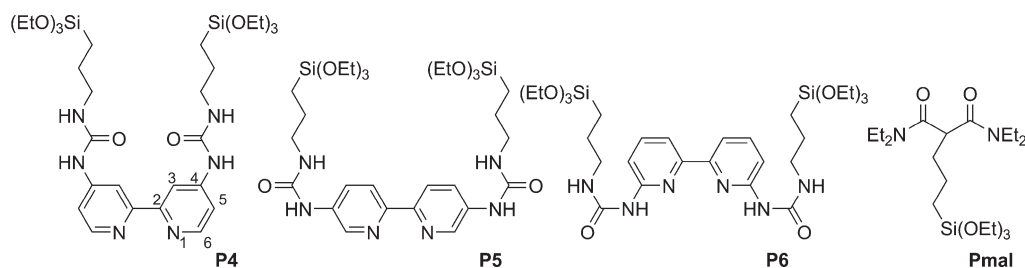
Figure 1. Chemical structure of the silylated precursors used in this study. The numbers denote the labeling of the atoms on the pyridine rings.

phosphors based on mesoporous silica incorporating Eu^{3+}- and Tb^{3+}-based complexes and organic ligands were recently reported.[15] Moreover, dense, homogeneous, well-oriented, and highly organized open-channel monolayers of zeolite L microcrystals have been synthesized using an organic—inorganic functional linker capable of coordinating and sensitizing Ln^{3+} ions.[16]

Thin films of Ln^{3+}-based hybrids prepared without any external template were also explored, although more scarcely. Silylated ligands, such as carboxylates,[17] diureasils,[18] and pyridine,[19] have been employed in a pure form. Most of the other examples in the literature reporting the fabrication of thin films of Ln^{3+}-based hybrids involve mixtures with TEOS or tetramethylorthosilicate (TMOS) and an organosilylated precursor.[20−27]

In these organic—inorganic hybrids, the organic fragment has a key role in complexing and sensitizing the Ln^{3+} ions. For this purpose, nitrogen-based chelating heterocycles have been widely used and, more particularly, Ln^{3+}-containing 4,4′-diureido-2, 2′-bipyridine-based bridged silsesquioxanes obtained from precursor **P4**[28] (Figure 1) have recently attracted considerable interest, in view of their potential use as optically active hybrid materials.[16,29−32]

Until now, only the 4,4′-isomer of this system has been studied. As the position of the ureido substituents on the 2,2′-bipyridine fragments (basicity, steric hindrance, chelation by urea groups),[33] should significantly impact on the light-emitting features of the Ln^{3+}-containing materials, we decided to investigate the effect of the substituent position on the bipyridine ring by synthesizing two new related precursors (denoted **P5** and **P6**; see Figure 1). Here, we report the preparation of Eu^{3+}- and Tb^{3+}-containing bridged silsesquioxanes obtained by hydrolysis—condensation of **P5** or **P6** in the presence of europium and terbium chloride and their photoluminescence (PL). In particular, we will focus on Eu^{3+}-containing hybrids derived from **P6** that can be processed as transparent and mechanically stable thin films with an intriguing potential as new LSCs.

2. EXPERIMENTAL SECTION

Synthesis. All the manipulations were carried out using Schlenk techniques under dry argon. Dry, oxygen-free solvents were employed. (3-isocyanatopropyl)triethoxysilane (ICPTES, Aldrich) and water were purified by distillation prior to use. Europium(III) chloride hexahydrate (99.99%) and terbium(III) chloride hexahydrate (99.9%) were purchased from Aldrich (Lot No. 203254) and Alfa Aesar, respectively. 6, 6′-Diamino-2,2′-bipyridine (purified by sublimation under vacuum),[34] **P4**,[28] and **Pmal**[35,36] were synthesized according to previously reported procedures.

5,5′-Diamino-2,2′-bipyridine.[37,38] A mixture of 5,5′-bis(2, 5-dimethylpyrrol-1-yl)-2,2′-bipyridine[38] (3.50 g, 10.2 mmol), hydroxylamine hydrochloride (21.3 g, 307 mmol), triethylamine (11.5 mL, 82 mmol),

ethanol (75 mL), and water (30 mL) was heated under reflux for 20 h. The mixture was cooled to room temperature then basified to pH 12, using a 1 M sodium hydroxide solution. After distilling off the triethylamine and ethanol at atmospheric pressure, the residual mixture was cooled to 4 °C for 3 h, yielding off-white crystals of 5,5′-diamino-2,2′-bipyridine dihydrate. These crystals were sublimed under vacuum to afford the pure 5,5′-diamino-2,2′-bipyridine as a white powder (1.60 g, 84% yield).

Synthesis of Precursors P*n* (*n* = 5 or 6). To a solution of *n*, *n*′-diamino-2,2′-bipyridine (1.50 g, 8.05 mmol) in freshly distilled pyridine (26 mL) was added under argon ICPTES (4.39 mL, 17.7 mmol). The mixture was heated at 60 °C for 2 days in a sealed Schlenk tube. After evaporation, washing with dry acetone (4 × 30 mL), and drying, the precursors **P*n*** were obtained as white powders. **P5** (5.13 g, 94% yield). ^{1}H NMR (dmso-d_6): δ (ppm): 0.57 (m, 4 H); 1.15 (t, J = 6.9 Hz, 18 H); 1.50 (m, 4 H); 3.08 (m, 4 H); 3.75 (q, J = 6.9 Hz, 12 H); 6.37 (br, 2 H); 7.98 (d, J = 8.6 Hz, 2 H); 8.14 (d, J = 8.6 Hz, 2 H); 8.57 (s, 2 H); 8.75 (s, 2 H). ^{13}C NMR (dmso-d_6): δ (ppm): 8.6; 19.5; 24.6; 43.2; 59.0; 120.9; 126.4; 138.2; 139.9; 149.6; 156.3. **P6** (4.77 g, 87% yield). ^{1}H NMR (dmso-d_6): δ (ppm): 0.62 (m, 4 H), 1.15 (t, J = 6.9 Hz, 18 H), 1.59 (m, 4 H), 3.25 (m, 4 H), 3.75 (q, J = 6.9 Hz, 12 H), 7.48 (d, J = 7.8 Hz, 2 H), 7.68 (d, J = 7.8 Hz, 2 H), 7.85 (t, J = 7.8 Hz, 2 H), 8.19 (s, 2 H), 9.31 (s, 2 H); ^{13}C NMR (dmso-d_6): δ (ppm): 11.2, 18.4, 24.8, 45.0, 58.5, 108.3, 113.6, 138.5, 151.7, 155.1, 158.6.

Synthesis of Hybrid Materials M*n*-Ln (*n* = 5 or 6; Ln = Eu, Tb). To a stirred suspension of **P*n*** (200 mg, 0.294 mmol) in dry ethanol (2 mL) at room temperature was added a mixture of water (155 μL, 8.61 mmol), ethanol (0.8 mL), and lanthanide chloride hexahydrate (9.7 10^{-2} mmol). A solution of ammonium fluoride (1 M in H_2O, 3 μL, 3 μmol) in ethanol (0.2 mL) was added after 10 min to this clear yellow solution (final molar ratio **P*n***/$LnCl_3$/H_2O/NH_4F = 1:0.33:32:0.01; final concentration of **P*n*** = 0.1 M). Precipitation of small particles occurred within 30 min. After 3 days of aging, the precipitate was filtered off, successively washed with water, ethanol and acetone (3 × 10 mL of each solvent) and finally dried at 80 °C for 12 h. White powders were obtained in all cases. *Elemental analyses:* **M5-Eu** (Si, 10.45; Eu, 1.42); **M6-Eu** (Si, 9.31; N, 12.95; Cl, 6.43; Eu, 9.25); **M6-Tb** (N, 13.38; Tb, 9.26).

M6′-Eu. A synthesis similar to that of **M6-Eu** was performed, from **P6** (200 mg, 0.294 mmol) europium chloride hexahydrate (55 mg, 0.15 mmol) water (155 μL, 8.61 mmol), and ammonium fluoride (1 M in H_2O, 3 μL, 3 μmol) (final molar ratio **P*n***/$EuCl_3$/H_2O/NH_4F = 1:0.50:33:0.01; final concentration of **P*n*** = 0.1 M). *Elemental analysis:* **M6′-Eu** (Si, 8.11; N, 12.25; Eu, 11.20).

M6-Eu-mal. A synthesis similar to that of **M6-Eu** was performed, from **P6** (200 mg, 0.294 mmol), **Pmal** (41 mg, 9.7 10^{-2} mmol), europium chloride hexahydrate (36 mg, 9.7 10^{-2} mmol), water (210 μL, 11.7 mmol), and ammonium fluoride (1 M in H_2O, 4 μL, 4 μmol) (final molar ratio **P*n***/**Pmal**/$EuCl_3$/H_2O/NH_4F = 1:0.33:0.33:42:0.01; final concentration of **P*n*** = 0.1 M). *Elemental analysis:* **M6-Eu-mal** (Si, 8.38; N, 11.98; Cl, 6.97; Eu, 7.08).

F6-Eu Thin Film. Borosilicate substrates (Normax microslides, 25 mm × 25 mm) were cleaned with acetone, immersed in a mixture of hydrogen peroxide and sulfuric acid, and rinsed and stored with distilled water. Prior to the deposition, they were dried by spin-coating (5 000 rpm, 50 s), treated with ethanol, and dried again by spin-coating just before use. Europium chloride hexahydrate (7.1 mg, 1.9×10^{-2} mmol) and water (31 μL, 1.7 mmol) were incorporated into a suspension of **P6** (40 mg, 5.9×10^{-2} mmol) in dry ethanol (2.5 mL). The mixture was stirred for 20 min at room temperature, leading to a clear solution; then, an ammonium fluoride solution (1 μL, 1 M in water) was added (final molar ratio **P6**/$EuCl_3$/H_2O/NH_4F = 1:0.33:32:0.01; final massic (weight) concentration of **P6** = 2%$_w$). The substrates were held by suction on a chuck, which was placed on the axis of the spin coater (SCS Specialty Coating Systems, spin-coat G3-8). The **F6-Eu** thin films were prepared by spin-coating two drops of the sol on glass substrates, with an acceleration time of 10 s and a spin time of 50 s, at a spin rate of 5000 rpm. They were finally dried at 80 °C for 10 h.

Fourier Transform Infrared (FT-IR) Spectroscopy. The FT-IR spectra were acquired between 400 and 4000 cm^{-1} at room temperature using a Mattson Mod 7000 spectrometer. The solid samples (3−4 mg) were finely ground, mixed with 300 mg of dried KBr (Merck, spectroscopic grade) and pressed into pellets, which were left for 24 h at 80 °C in order to reduce the level of absorbed water before use.

Nuclear Magnetic Resonance (NMR). Nuclear magnetic resonance (NMR) spectra were recorded at 298 K on a Bruker Model Advance 400 apparatus. ^{1}H and ^{13}C chemical shifts are reported in units of ppm, relative to Me_4Si.

Powder X-ray Diffraction (XRD). X-ray diffraction (XRD) measurements of the dried powder samples were carried out in 1.5-mm-diameter glass capillaries in a transmission configuration at the LCVN Laboratory (Montpellier, France). A copper rotating-anode X-ray source working at 4 kW with a multilayer focusing Osmic monochromator, giving high flux and punctual collimation, was employed. A two-dimensional (2D) image plate detector was used.

Scanning Electron Microscopy (SEM). Scanning electron microscopy (SEM) images were obtained with a Hitachi Model S-4800 apparatus after platinum metallization.

Optical Imaging. Optical micrographs were acquired with a Leica Model DM6000 M microscope. The images were obtained through a 2592 × 1944 pixel CCD Leica Model DFC425C camera. Photographs were taken with a digital camera (Canon Model EOS 400D), using an exposure time between 6 and 20 s. Excitation of the film was performed with a Spectroline E-Series UV lamp (Aldrich, Model Z169625) operating at 254 and 365 nm. The spectral intensity maps were performed using the MATLAB programming language, considering the RGB model to determine the intensity value of the red pixels (ranging from 0 to 255). In order to quantify the emission ratio factor (*C*), cross-sectional intensity profiles of the pixels (red intensity values) were measured in different planes of six film images. The photographs used to calculate the intensity maps were acquired with exposure times between $^1/_{20}$ s and 2.5 s to avoid saturation of the intensity of the red pixels.

Elemental Analysis. Elemental analyses of the hybrids were performed by the Service Central d'Analyses du CNRS (Lyon, France). The experimental errors are ±0.4% (absolute) for chlorine, ±0.3% (absolute) for nitrogen, and ±2% (relative error) for europium and silicon. Europium and silicon contents were determined by ICP-AES after alkaline digestion, whereas chlorine and nitrogen contents were determined after combustion.

Ultraviolet−Visible (UV−vis) Absorption Spectroscopy. Ultraviolet−Visible (UV−vis) absorption spectra were measured on a JASCO Model V-560 spectrometer with a scan range of 200−900 nm, with a scan rate of 200 nm min^{-1} and a resolution of 0.5 nm. A clean substrate was used as reference in order to eliminate the substrate contribution in the absorption spectra of the film.

Photoluminescence. The photoluminescence (PL) spectra were recorded at 10 and 300 K and room temperature with a modular double-grating excitation spectrofluorimeter with a TRIAX 320 emission monochromator (Fluorolog-3 2-Triax, Horiba Scientific) coupled to a R928 Hamamatsu photomultiplier, using the front face acquisition mode. The excitation source was a 450-W xenon arc lamp. The emission spectra were corrected for detection and optical spectral response of the spectrofluorimeter and the excitation spectra were weighed for the spectral distribution of the lamp intensity using a photodiode reference detector. The time-resolved measurements were acquired with the setup previously described for the PL spectra, using a pulsed Xe-Hg lamp (6 μs pulse at half width and 20−30 μs tail).

Absolute Emission Quantum Yields. The absolute emission quantum yields were measured at room temperature using a quantum yield measurement system (Model C9920-02, from Hamamatsu, with a 150-W xenon lamp coupled to a monochromator for wavelength discrimination), an integrating sphere as the sample chamber, and a multichannel analyzer for signal detection. Three measurements were made for each sample, so that the average value is reported. The method is accurate to within 10%.

Ellipsometry. The spectroscopic ellipsometry measurements were made using an AutoSE ellipsometer (Horiba Scientific) with a total of 250 points in the wavelength interval of 440−850 nm, an incidence angle of 70°, an acquisition time of 22 ms per point, and an average of 10 measurements per point. Refractive index of the film were calculated using the Lorentz model, which expresses the relative complex dielectric constant as a function of the frequency (ω), which is described by

$$\varepsilon = \varepsilon_\infty + \frac{(\varepsilon_s - \varepsilon_\infty) \times \omega_0^2}{(\omega_0^2 - \omega^2) + i\Gamma\omega} \tag{1}$$

where ε_∞ is the high-frequency relative dielectric constant, ε_s the static relative dielectric constant, ω_0 (eV) the oscillator resonant frequency, and Γ (eV) the damping factor.[39] The fit method was detailed elsewhere.[40]

3. RESULTS AND DISCUSSION

The three organosilane precursors—**P4**−**P6**—were obtained in good to excellent yield from the corresponding *n,n′*-diamino-2,2′-bipyridine by reaction with (3-isocyanatopropyl)triethoxy-silane in hot pyridine.[28] Their hydrolysis—condensation in the presence of europium chloride was investigated for different compositions. To evaluate the effect of the ureido substituent's positions on the luminescence properties, we will discuss, in the first part of the manuscript, the synthesis and PL of the **M5-Eu** and **M6-Eu** bulk materials obtained under the same conditions as the previously reported **M4-Eu**.[31] In the second part of the work, we will optimize the optical properties of the materials, by modifying the composition of the sol, describing the processing of highly luminescent thin films obtained by spin-coating, with the potential impact of new luminescent solar concentrators (LSCs).

3.1. Synthesis and Characterization of the M5-Eu and M6-Eu Bulk Materials. For comparison purposes, we prepared a first set of **P4**, **P5**, and **P6**-derived materials under similar conditions. Materials **M*n*-Ln** were obtained as bulk samples from a homogeneous solution of **P*n***, $LnCl_3 \cdot 6H_2O$, solvent (methanol or ethanol), NH_4F and water (**P*n***/$LnCl_3 \cdot 6H_2O$/H_2O/NH_4F = 1:0.33:30:0.01 at 0.1 M in dry methanol (**M4-Ln**) or ethanol (**M5-Ln**, **M6-Ln**)). Interestingly, whereas the precursors were sparingly soluble in the alcoholic solvents, the introduction of the lanthanide salt to these suspensions immediately led to complete solubilization, indicating that complexation had occurred between

Table 1. Elemental Composition and Calculated Molar Ratios for the Different Materials Studied[a]

hybrid	Composition (%w)				Si/Eu	N/Ln	Cl/Eu	N/Si
	Si	N	Ln	Cl				
M6-Eu	9.31	12.95	9.25	6.43	5.4 (6)	15.2 (18)	3.0 (3)	2.8 (3)
M6′-Eu	8.11	12.25	11.20	nd[b]	3.9 (4)	11.9 (12)	nd[b]	3.0 (3)
M6-Tb	nd[b]	13.38	9.26	nd[b]	nd[b]	16.7 (18)	nd[b]	nd[b]
M6-Eu-mal	8.38	11.98	7.08	6.97	6.4 (7)	18.4 (20)	4.2 (3)	2.9 (2.8)
M5-Eu	10.45	nd[b]	1.42	nd[b]	39.9 (6)	nd[b]	nd[b]	nd[b]
M4-Eu (ref 31)	8.29	14.10	4.98	nd[b]	9.0 (6)	30.7 (18)	nd[b]	3.4 (3)

[a] Values given in parentheses indicate the theoretical ratio. [b] Not determined.
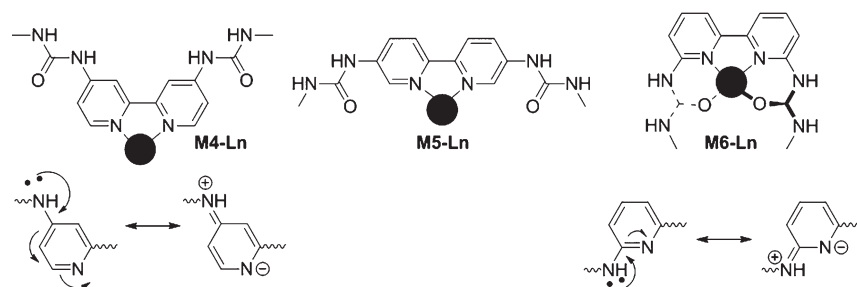

Figure 2. (Top) Schematic representation of the possible interactions between the Ln ion (full circle) and one diureido-2,2′-bipyridine ligand. (Bottom) Mesomeric formulas involving the pyridine nitrogen atoms.

the europium salt and the bipyridine-based precursors. After addition of the ammonium fluoride catalyst, gelation (**M4-Ln**) or precipitation (**M5-Ln**, **M6-Ln**) occurred.

Figure S1 in the Supporting Information depicts the FT-IR spectra of all the materials, which are all very similar. The formation of the siloxane skeleton was ascertained by the appearance of a broad band (975−1140 cm^{-1}) with two main components located at 1020 and 1140 cm^{-1} (ν_{as}(SiOSi)). A characteristic band at 905 cm^{-1}, attributable to noncondensed Si−OH groups, is also observed, giving evidence that the condensation is not complete. However, since no ^{29}Si solid-state NMR spectrum could be recorded, because of the paramagnetism of the Eu^{3+} ions, it is difficult to precisely evaluate the condensation at Si. The broad bands centered at 1550, 1605, and 1668 cm^{-1} result from the contributions of the vibrations in the pyridine rings and of the amide I and amide II modes of the urea groups. This gives clear evidence for the presence of the organic fragments within the material.

The elemental analyses (Table 1) performed on the different materials indicate that the N/Si ratio is similar (within the experimental error) to the expected values, thus further confirming the preservation of the organic component within the hybrid materials. These analyses give also very good indications of the complexing ability of precursors **P**n (n = 4, 5, or 6): whereas **M6-Eu** contains as much as 9.2%w of europium (the theoretical value for all these europium-containing materials in the case of a complete condensation is 9.3%w), the corresponding amount is reduced to 5.0%w in **M4-Eu**, and only 1.4%w in the case of **M5-Eu**. This corresponds to bpy/Eu ratios of 5:1, 20:1, and 3:1, for **M4-Eu**, **M5-Eu**, and **M6-Eu**, respectively. The low amount of europium incorporated in **M5-Eu** may result from the low basicity of the 5,5′-diureido-2,2′-bipyridine ligand, compared to the other isomers (as inferred from the mesomeric formulas

depicted in Figure 2), and also from the good packing ability of the linear monomers that would disfavor the formation of bulkier europium complexes. In contrast, the full incorporation of the Ln^{3+} salt in **M6-Eu** and **M6-Tb** might come from the chelation of the Ln ion by both the urea and bipyridine moieties, with the formation of a cagelike complex, as illustrated in Figure 2. Moreover, the preservation of a Cl/Eu molar ratio of 3.0 in **M6-Eu** demonstrates that no anion exchange occurred during the sol−gel process.

XRD experiments performed on the dried powders exhibit two very broad bands, peaking at ∼5.7−5.9 nm^{-1} and ∼15.5−15.7 nm^{-1} (see Figure S2 in the Supporting Information), which indicates nonorganized structures, even for **M5-Eu**. Notably, no sharp lines typical of inorganic crystals that would show a phase segregation between lanthanide salts and the hybrid materials[41] could be detected.

Different morphologies were observed for these materials by SEM (Figure 3): whereas **M4-Eu** exhibits a featureless morphology,[31] the structure of **M5-Eu** can be described as an assembly of tiny spheres (<100 nm in size). Interestingly, **M6-Eu** and **M6-Tb** are obtained as aggregates of microspheres (1−4 μm in diameter) that are also observable by optical microscopy (see Figure S3 in the Supporting Information).

The PL of these hybrid materials was investigated using various techniques (steady-state and time-resolved emission, excitation, and emission quantum yield measurements). For **M6-Tb**, the intra-4f lines could not be discerned and the emission spectrum is formed only by a host-related broad component (see Figure S4 in the Supporting Information and discussion below). The host-to-metal energy transfer is hindered by the high-energy location of the Tb^{3+} ^{5}D$_4$ emitting level, relative to the ligands exciting states, and then we will focus on the Eu^{3+}-containing hybrids. Figure 4A depicts the emission features of **M5-Eu** and

M6-Eu, under the excitation wavelength that maximizes the emission intensity. In order to study the effect of the substituents' position on the PL features the spectrum of **M4-Eu** is also presented.[29,31] All the spectra display the Eu^{3+} $^5D_0 \rightarrow {}^7F_{0,4}$ transitions and a broad band (400–550 nm), most evident for **M5-Eu**, whose energy depends on the excitation wavelength (see Figure S5 in the Supporting Information). The broad band resembles that observed for the **M4-Eu**[31] and pristine **M4**[42] hybrids, being ascribed to the superposition of three distinct components: the bpy-related triplet state and electron–hole recombinations originated in the urea groups cross-linkages and in the siliceous nanoclusters.[42] The Eu^{3+}-excitation paths were selectively studied by measuring the excitation spectra monitored
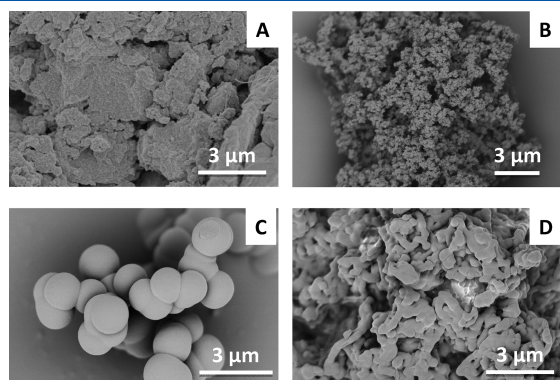
within the $^5D_0 \rightarrow {}^7F_2$ transition (see Figure 4B). The spectra reveal a large band in the UV/blue spectral region with two main components, at 277 nm and 363–373 nm, and a low-relative intensity band between 360 and 450 nm (more evident in the excitation spectrum of **M5-Eu**). A similar excitation spectrum was already observed for the analogous **M4-Eu**[31] hybrid (curve c in Figure 4B). Whereas the low-wavelength region (240–360 nm) is related to the excited states of the bpy-ligands, the high-wavelength one (360–450 nm) is associated with the excited states of the NH/C=O groups and of the siliceous nanoclusters.[43,44] The presence of both the bpy and hybrid host excited states in the excitation spectra monitored within the Eu^{3+} excited states points out the presence of bpy/hybrid→Eu^{3+} energy transfer, as also noted for **M4-Eu**.[31] The different energy values of the excitation components and the distinct relative intensity of the intra-4*f* lines suggest that the nature of the isomer plays an active role in the Eu^{3+} sensitization.

The emission features were quantified through the measurement of the absolute emission quantum yields (Table 2). Maximum quantum yield values of 0.01 ± 0.001 (280 nm) and 0.18 ± 0.02 (350 nm) were measured under excitation via the bpy-related excited states for **M5-Eu** and **M6-Eu**, respectively. The quantum yield value previously reported for the **M4-Eu** is 0.08 ± 0.01 (320 nm). The significant difference between those values points out the crucial role of the ureido substituents' positions in the PL features.

In order to gain some insight into the Eu^{3+}-local coordination of the **M5-Eu** and **M6-Eu** hybrid hosts, the Eu^{3+}-lines were measured with high resolution (Figure 5). The energy and full width at half-maximum (fwhm) of the intra-4*f*[6] transitions in the
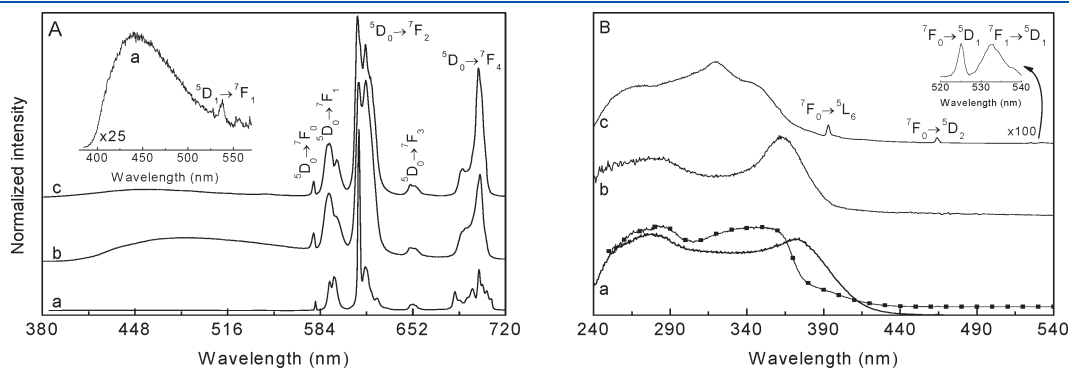

Figure 3. SEM images of (A) **M4-Eu**, (B) **M5-Eu**, (C) **M6-Eu**, and (D) **M6-Eu-Mal**.

Figure 4. (A) Emission and (B) excitation spectra (300 K) of (a) M6-Eu, (b) M5-Eu, and (c) M4-Eu monitored at 612 nm and excited at 373, 363, and 320 nm, respectively. The solid line with squares corresponds to the excitation spectra of M6-Eu monitored at 616 nm. The insets show a magnification of the broad band emission of M6-Eu (spectrum a) and of the $^7F_{0,1} \rightarrow {}^5D_1$ transitions of M4-Eu (spectrum c).

Table 2. E_{00}, Full Width at Half Maximum (fwhm$_{00}$), $^5D_0$ Lifetime (τ), and Maximum Absolute Emission Quantum Yields[a] of All the Eu^{3+}-Containing Bridged Silsesquioxanes

	E_{00} (cm^{-1})		Full Width at Half Maximum, fwhm$_{00}$ (cm^{-1})		τ (ms)		
hybrid	Site 1	Site 2	Site 1	Site 2	Site 1	Site 2	$\phi(\lambda_{ex}$ (nm))
M4-Eu (ref 31)	17270.8 ± 0.4				0.384 ± 0.016		0.08 ± 0.02 (320)
M5-Eu	17270.5 ± 0.5		56.1 ± 1.2		0.483 ± 0.005[b]		0.01 ± 0.001(280)
M6-Eu	17270.0 ± 3.3	17224.2 ± 0.2	61.5 ± 5.9	25.0 ± 0.5	0.313 ± 0.009	0.863 ± 0.013	0.18 ± 0.02 (350)
M6′-Eu	17242.6 ± 1.9	17223.0 ± 0.11	42.6 ± 1.9	19.3 ± 0.3	0.300 ± 0.020	0.850 ± 0.039	0.19 ± 0.02 (350)
M6-Eu-mal	17237.7 ± 1.1	17223.9 ± 0.2	45.1 ± 1.1	21.6 ± 0.5	0.309 ± 0.014	0.871 ± 0.016	0.26 ± 0.03 (350)
F6-Eu	17239.4 ± 1.1	17223.6 ± 0.1	50.4 ± 1.4	21.0 ± 0.3	0.301 ± 0.014	0.860 ± 0.071	0.34 ± 0.03(350)

[a] The excitation wavelength is indicated in parentheses. [b] Average lifetime ($\langle \tau \rangle$).
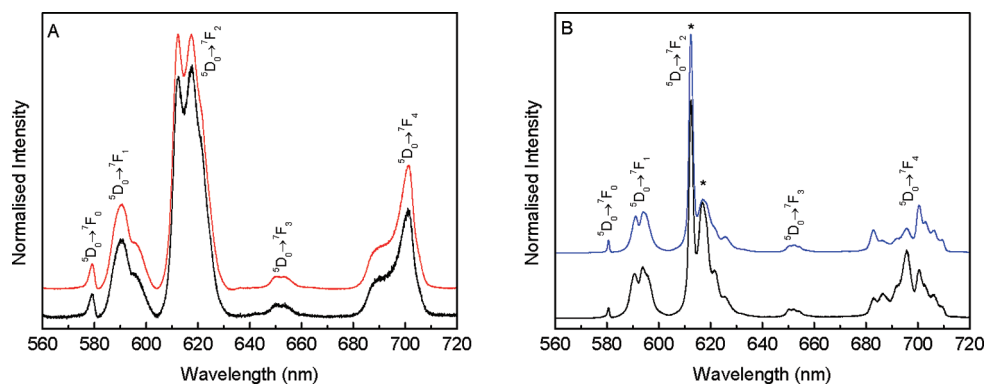
Figure 5. High-resolution emission spectra (300 K) of (A) **M5-Eu** and (B) **M6-Eu** excited at 277 nm (black line), 363 nm (red line), and 373 nm (blue line).

emission spectra of **M5-Eu** are almost independent of the excitation wavelength. Moreover, a single $^5D_0 \rightarrow ^7F_0$ line and a J-degeneracy splitting of the $^7F_{1,2}$ levels into three and four Stark components, respectively, are observed, indicating that the Eu^{3+} ions occupy a low symmetry site without an inversion center, in accordance with the higher intensity of the electric-dipole $^5D_0 \rightarrow ^7F_2$ transition.[45] Nevertheless, the emission spectra of **M6-Eu** show major changes in the energy, fwhm, and relative intensity of the $^5D_0 \rightarrow ^7F_{0-4}$ lines under distinct excitation wavelengths (see Figure 5), pointing out the presence of at least two Eu^{3+} average local environments. This emission dependence on the excitation wavelength is mostly evident in the relative intensity variation of the $^5D_0 \rightarrow ^7F_2$ Stark components at 612 and 616 nm (marked with an asterisk in Figure 5) as the excitation wavelength increases from 277 nm to 373 nm. In order to study the excitation path of each Eu^{3+} local site selectively, the excitation spectrum monitored at 612 nm was compared with that monitored at 616 nm (see Figure 4B). Although the low-wavelength regions of the two spectra overlap, the high-wavelength components are blue-shifted (ca. 2050 cm^{-1}), supporting the presence of two distinct Eu^{3+} local environments, as previously mentioned.

The Eu^{3+} local coordination, as function of the position of the two urea substituents on the bipyridine fragments was further analyzed through the estimation of the energy (E_{00}) and full-width at half maximum (fwhm$_{00}$) of the $^5D_0 \rightarrow ^7F_0$ transition (see Figure S6 in the Supporting Information). The $^5D_0 \rightarrow ^7F_0$ transition of the **M5-Eu** spectrum is well-reproduced by a single Gaussian function, yielding E_{00} = 17270.5 ± 0.5 cm^{-1} and fwhm$_{00}$ = 56.1 ± 1.2 cm^{-1} (see Table 2). To simplify the discussion, this Eu^{3+} local site will be hereafter referenced as "Site 1". Despite the presence of a single $^5D_0 \rightarrow ^7F_0$ line, the large fwhm$_{00}$ value suggests a higher nonhomogeneous distribution of similar Eu^{3+} Site 1 chemical environments, because of changes outside the coordination polyhedron.

The E_{00} value is the same as that reported for **M4-Eu** (E_{00} = 17270.8 ± 0.4; see Table 2), suggesting an analogous Eu^{3+} local coordination in both **M4** and **M5** hybrids, in agreement with the proposed schematic representation of the possible Eu^{3+}-to-diureido-2,2′-bipyridine ligand interactions (see Figure 2). Nevertheless, the significant increase in the fwhm$_{00}$ value, relative to that of **M4-Eu** (fwhm$_{00}$ = 41.6 ± 0.9 cm^{-1}; see Table 2), reflects a larger distribution of related Eu^{3+} local coordination sites.

The $^5D_0 \rightarrow ^7F_0$ transition of the **M6-Eu** spectrum was modeled by the sum of two Gaussian functions displaying one component with E_{00} = 17270.0 ± 3.3 cm^{-1} and fwhm$_{00}$ = 61.5 ± 5.9 cm^{-1}, comparable to that measured for **M4-Eu** and **M5-Eu** and

therefore ascribed to Site 1, and another component characterized by lower values of E_{00} and fwhm$_{00}$ (E_{00} = 17224.2 ± 0.2, fwhm$_{00}$ = 25.0 ± 0.5 cm^{-1}), which will be denoted hereafter as "Site 2". The lower energy of the $^5D_0 \rightarrow ^7F_0$ transition of Site 2 indicates that the Eu-ligand bonds have (on average) a high covalent character, relative to that found in Site 1.[46,47] This is in good agreement with the main coordination type proposed in Figure 2 for the **P6**-related hybrids, which involves both the N atoms of the bpy-ligands (which are also involved in Site 1 coordination) and the O atoms of the urea groups.

The $^5D_0$ lifetime values were estimated by measuring the emission decay curves within the $^5D_0 \rightarrow ^7F_2$ transition excited via the bpy/hybrid-related broad band (277 nm). The $^5D_0$ emission decay curve of **M5-Eu** reveals a nonsingle exponential behavior (see Figure S7 in the Supporting Information), which can be attributed to the large distribution of Eu^{3+} local sites, as mentioned above. Therefore, an average lifetime value ($\langle \tau \rangle$) was estimated, considering

$$\langle \tau \rangle = \frac{\int_{t_0}^{t_1} I(t) t \, dt}{\int_{t_0}^{t_1} I(t) \, dt} \tag{2}$$

where $t_0 = 0$ and t_1 is the time interval where the luminescence intensity ($I(t)$) reaches the background, yielding ~0.483 ± 0.005 ms. For **M6-Eu**, the emission decay curves are well-reproduced by a biexponential function, in good agreement with the presence of two Eu^{3+} local sites, yielding lifetime values of 0.313 ± 0.009 ms and 0.863 ± 0.013 ms (see Figure S8 in the Supporting Information).

The emission features of **M5-Eu** and **M6-Eu** were also studied at a temperature of 10 K. Whereas the PL features of **M5-Eu** resemble those acquired at room temperature, for **M6-Eu**, the emission data at 10 K is almost independent of the excitation wavelength (see Figure S9 in the Supporting Information), and only the $^5D_0 \rightarrow ^7F_0$ component of Site 2 is detected (E_{00} = 17224.5 ± 0.1, fwhm$_{00}$ = 21.4 ± 0.1 cm^{-1}), suggesting that Site 1 is thermally activated in **M6-Eu**. The selective emission of Site 2 at 10 K is corroborated by the emission decay curves (monitored within the $^5D_0 \rightarrow ^7F_2$ transition) which are well-reproduced by a single exponential function (see Figure S10 in the Supporting Information), yielding a lifetime value of 1.064 ± 0.008 ms. Comparing this value with those measured at 300 K, we tentatively assign the low and high lifetime values to the $^5D_0$ level of Eu^{3+} in Site 1 and Site 2 (see Table 2).
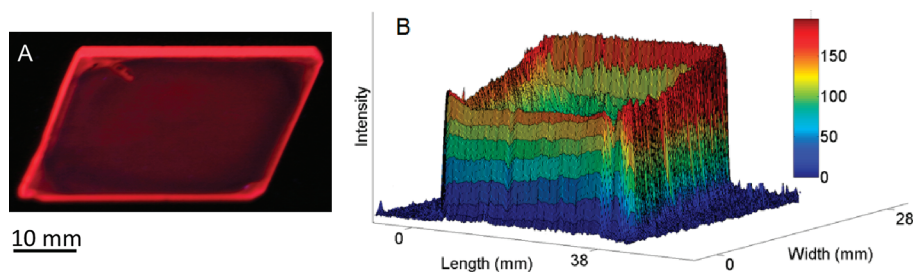
Figure 6. (A) Photograph and (B) intensity map of the red pixel of **F6-Eu** excited at 365 nm. The top edge of the photograph corresponds to the more-intense profile in the intensity map.
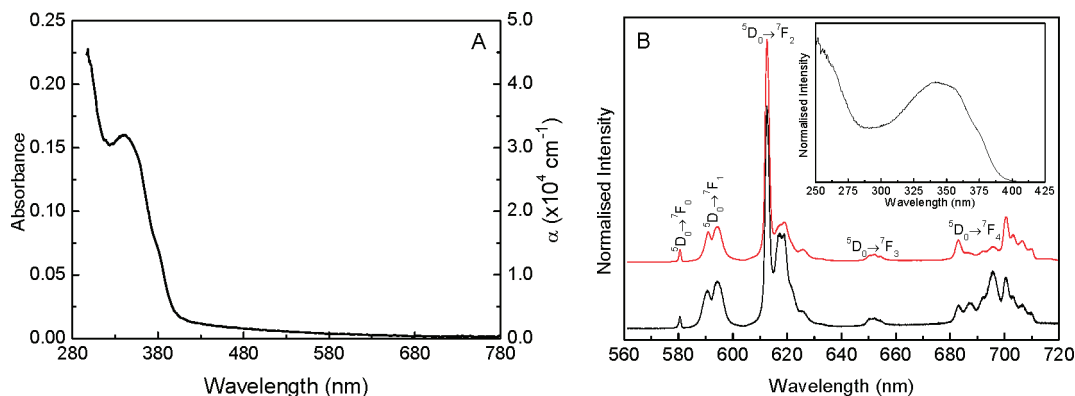

Figure 7. (A) UV–vis absorption spectrum and (B) high-resolution emission spectra (300 K) excited at 277 nm (black line) and 373 nm (red line) of **F6-Eu**. The inset shows the excitation spectrum (300 K) monitored at 612 nm.

3.2. Optimization of the Materials and Processing as Thin Films. Since **M6-Eu** is the most efficient material among the three isomers of the Eu^{3+}-containing bridged silsesquioxanes investigated in this work, we focused our efforts on materials derived from **P6** to optimize the formulation of the luminescent hybrids. The first modification implies an increase in the Eu^{3+} contents in the materials: the hybrid material **M6′-Eu** was synthesized with the bpy/$EuCl_3$ ratio of 2:1 instead of 3:1 for **M6-Eu**. Elemental analysis (Table 1) evidences the full Eu^{3+} incorporation into the hybrid host, where a loading as high as $11.2\%_w$ was reached without any detectable phase separation by XRD. The second modification consists of the incorporation of an additional silylated precursor featuring the tetraethylmalonamide moiety (**Pmal**; see Figure 1),[35,36] to increase the UV-harvesting absorption and trying to saturate the Ln^{3+} coordination shell yielding material M6-Eu-mal. Indeed, the malonamide fragment is a good ligand for lanthanides and actinides and can coordinate the cation in a monodentate or bidentate fashion.[48]

Interestingly, all the spectroscopic features of **M6′-Eu** and **M6-Eu-mal** are very similar to those of **M6-Eu** (see Figures S1 and S2 in the Supporting Information). Furthermore, although the morphology of the former is very similar to that of **M6-Eu**, the latter is obtained in a wormlike form, probably resulting from the agglomeration of small spheres (Figure 3). In addition, the sol yielding **M6-Eu** could easily be spin-coated into transparent luminescent thin films (**F6-Eu**) (see Figure 6 and Figure S11 in the Supporting Information) with a thickness value (d) of ∼54 nm, determined by ellipsometry measurements, vide infra. As far as we know, only Dong et al.[17,49] and Chamas et al.[19] spin-coated pure silylated precursors, as we describe here, whereas Wang et al.[50,51] reported films of Ln^{3+}-containing bridged silsesquioxanes

from powder precipitation on a glass substrate. The emission quantum yield measured for **F6-Eu** (0.34 ± 0.03) is among the highest values ever reported for films of Eu^{3+}-containing hybrids (see Table 3 of ref 3). To date, only very few examples of organic–inorganic hybrids, all made with TMOS, are known: (TMOS)/3-glycidoxypropyltrimethoxysilane and TMOS/diethoxydimethylsilane doped with $[Eu(tta)_3(H_2O)_2]$ (tta = thienoyltrifluoroacetonate), with values between 0.12 ± 0.02 and 0.34 ± 0.02,[20] and also with TMOS, pluronic P123, $EuCl_3 \cdot 6H_2O$, 1,10-phenanthroline, and salicylic acid, with values between 0.04 and 0.29.[15] The absorption coefficient, $\alpha = A/d$ (and the corresponding UV–vis absorbance A of **F6-Eu**), is very low in the visible spectral range (wavelengths of >400 nm), reaching a maximum at ∼350 nm (see Figure 7A) (α is not recorded for wavelengths lower than 297 nm, because the glass substrate displays a very high absorbance in that spectral region).

The excitation (monitored within the $^5D_0 \rightarrow {}^7F_2$ transition) and emission spectra of **M6′-Eu** (see Figures S12 and S13 in the Supporting Information), **M6-Eu-mal** (Figures S12 and S14 in the Supporting Information), and **F6-Eu** (Figure 7B) resemble those acquired for **M6-Eu** (see Figures 4 and 5). The only difference is observed in the excitation spectrum of **F6-Eu** (the inset in Figure 7B), which displays a blue-shift (∼2200 cm^{-1}), relative to that measured for **M6-Eu**, which could be ascribed to differences in the gelification and condensation rates between the spin-coating process in the film and the sol–gel reactions in the monoliths. For thin films, the forced solvent extraction is much faster, compared with that of bulk monoliths, resulting in a structure with a lower degree of organization. This distortion on the symmetry could cause the change in the energy levels positions of the hybrid host and, consequently, the blue-shift in the thin film excitation spectrum.[18]

In order to discuss the effects on the Eu^{3+} local coordination in more detail, the energy and fwhm of the two components of the $^5D_0 \rightarrow ^7F_0$ transition were fitted by a sum of two Gaussian functions (see Figure S6 in the Supporting Information). It is observed that the variation of the bpy/Eu^{3+} ratio (9.2%$_w$—11.2%$_w$ Eu), the incorporation of the malonamide fragments and the thin-film processing induce no changes in the E_{00} and fwhm$_{00}$ values of Site 2. In contrast, for Site 1, a decrease in the fwhm$_{00}$ and a red-shift in the E_{00} are detected, pointing out that the Eu^{3+} local coordination at Site 1 is more affected than the local coordination involving both bpy and urea ligands (Site 2). The similarities between the emission features are reinforced by the $^5D_0$ emission decay curves (see Figures S15—S17 in the Supporting Information), which are well-reproduced by a biexponential function with time decay constants similar to those measured for **M6-Eu** (see Table 2).

The effect of the three modifications was also monitored in the emission quantum yield values: whereas no significant changes were observed with the increase in Eu^{3+} concentration, **M6-Eu-mal** and the **F6-Eu** film display a significant increase in the maximum values of the emission quantum yield (0.26 ± 0.03 and 0.34 ± 0.03, respectively; see Table 2), relative to **M6-Eu**. We should note that as the excitation spectra of **M6-Eu** and **M6-Eu-mal** that are monitored within the $^5D_0 \rightarrow ^7F_2$ transition are identical (see Figure S12 in the Supporting Information), thus indicating comparable $^5D_0$ excitation paths in the presence and absence of malonamide, we may suggest the presence of efficient malonamide$\rightarrow$bpy$\rightarrow$$Eu^{3+}$ energy transfer, which confirms that the malonamide fragments act as active additional UV-harvesting moieties. Contrary to its expected role, the PL features of **M6-Eu-mal** tend to indicate that the malonamide fragment is not directly coordinated to the Eu^{3+} ions, although it may figure in the second coordination shell.

In addition, the **F6-Eu** thin films were characterized by spectroscopic ellipsometry. The film thickness and the refractive index dispersion curve were measured, considering a layered structure model that was composed of the substrate, an organic–inorganic hybrid layer, and air as ambient medium (see Figure S18A in the Supporting Information). The thickness of the substrate was considered infinite, and the refractive index was obtained by direct inversion of the ellipsometric data (not shown). The experimental ellipsometric parameters and the respective fit using the Lorentz model are shown in Figure S18B in the Supporting Information. For an illustrative example, the best-fit solution yielded a thickness value of $d = 53.84 \pm 1.57$ nm and the refractive index variation represented in Figure 8. The presence of surface roughness was modeled by the Bruggemann effective medium approximation,[52] using the thickness (average roughness) of a layer composed of air and hybrid material. The improvement in the goodness of fit is <5%, yielding roughness values of ~0.1 nm, pointing out that surface irregularities can be neglected in the present case, despite the presence of small cubic nanoparticles shown in the SEM image (see Figure S19 in the Supporting Information) of the surface of the hybrid. The potential effect of the cubic nanometric particles and roughness in the ellipsometric spectra is depolarization of the reflected light, because of the scattering of the incident light by these surface features, which originates light reflected in more than one polarization states.[53] The measured depolarization spectrum shows a very small depolarization effect with a polarization degree very close to the unit (see inset in Figure 8). The poor effect of the surface nanoparticles in the ellipsometric analysis can be explained by two main reasons: (i) the surface
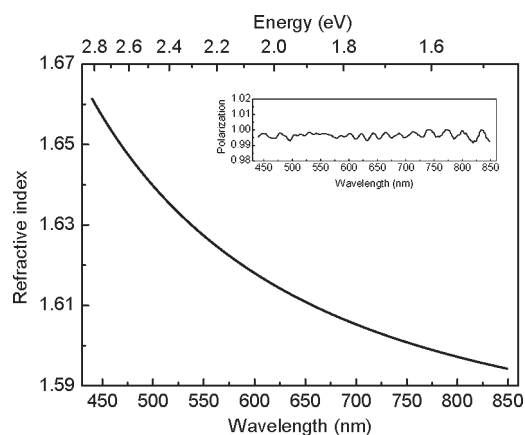

Figure 8. Refractive index variation, as function of the wavelength of **F6-Eu**. The inset shows the depolarization spectrum.

fraction occupied by the nanometer-size particles is very small (the contribution of the remaining surface is largely predominant) and (ii) the dimension of the nanometric particles itself is also very small, and, therefore, its effect could be neglected. Consequently, the values of the roughness measured by ellipsometry and the presence of the cubic nanoparticles in the surface of the hybrid are not in contradiction.

The photograph of the **F6-Eu** film under UV light at 365 nm (Figure 6A) shows the emitted intra-4f^6 red light to be guided to the film edges through internal reflection, revealing that the **F6-Eu** film can be used as LSC. To quantify the emission ratio factor C, we performed an intensity map of the red pixel (in the RGB color model) in nonsaturated photographs (not shown). Figure 6B displays one example of such three-dimensional (3D) intensity maps. In order to separate the contribution of the thin film emission and that of the scattered light at the surface, part of the film was removed from the substrate and the red pixel intensity at the film and at the substrate was estimated. This experiment enables a quantification of the scattered light of ~20% at 350 nm. Therefore, the average intensity ratio between corrected I_{sf} and I_e yields $C = 6$. This value is consistent with that reported for LSCs based on poly(methyl methacrylate) encapsulating organic dyes and quantum dots (QDs), with C values of 5—10.[12]

The performance of the **F6-Eu** thin film as a LSC is given by the optical conversion efficiency η_{opt} of the collector, which is defined as[8,11,13]

$$\eta_{opt} = (1 - R)\eta_{abs}\eta_f\eta_s\eta_t\eta_{tr}\eta_{self} \quad (3)$$

where R is the reflectance, η_{abs} is the ratio of photons absorbed by the plate to the number of photons falling on the plate, η_f is the emission quantum yield, η_s is the Stokes efficiency (ratio of the average energy of emitted photons to the average energy of the absorbed ones), η_t is the trapping efficiency, $\eta_t = (1 - 1/n^2)^{1/2}$ (where n is the refractive index of the light-emitting medium), η_{tr} is the transport efficiency (which takes into account the transport losses due to matrix absorption and scattering), and η_{self} is the self-absorption efficiency arising from self-absorption of the emitters. At 350 nm, the η_{opt} value of **F6-Eu** is initially estimated as ~4.3%, considering $R = 0.067$ (with the refractive index value at 350 nm, $n = 1.7006$, extrapolated from the dispersion curve of Figure 8), $\eta_{abs} = (1 - 10^{-A}) = 0.30$ (where A is the absorbance (0.153; see Figure 8)), $\eta_f = 0.34$, $\eta_s = 0.572$ (the emitted photons at 612 nm dominate), $\eta_t = 0.786$ ($n = 1.6161$ at 612 nm), and $\eta_{tr} = \eta_{self} = 1$,

4780

dx.doi.org/10.1021/cm2019026 |*Chem. Mater.* 2011, 23, 4773–4782

because the hybrid matrix is almost transparent to UV−vis light and Eu^{3+} ions have negligible self-absorption (no losses). The optical conversion efficiency of **F6-Eu** is smaller than that recorded for LSCs formed by a PMMA layer containing Red 305 dyes on top of a transparent glass support (~12%) and the upper estimate reported for films of Tb^{3+}-based poly(vinyl alcohol) incorporating salicylic acid (8.8%),[8] the only value that we found in the literature for LSCs based on Ln ions. However, in this latter example, η_{abs} is assumed to be equal to 1 (3-fold larger than that in **F6-Eu**). We certainly can improve the optical conversion efficiency of the **F6-Eu** film, by increasing its thickness and, consequently, its absorbance.

The emission ratio factor (C) could be also defined as

$$C = \left(\frac{\eta_{opt}}{\eta_{sf}/2}\right)\frac{A_{sf}}{A_e} = \left(\frac{2\eta_t}{1-\eta_t}\right)\frac{A_{sf}}{A_e} \qquad (4)$$

where

$$\eta_{sf} = (1-R)\eta_{abs}\eta_f\eta_s\eta_t(1-\eta_{tr})\eta_{self} \qquad (5)$$

is the conversion efficiency of the signal emitted at the surface of the film (in which the trapping efficiency is replaced by its complementary value, $(1-\eta_t)$); A_{sf} and A_e are the surface area and the area of the plate edges, respectively; and the factor $^1/_2$ takes into account that we are considering the emission trapping in only one film surface. For **F6-Eu**, the ratio between A_{sf} and A_e, known as the LSC geometrical factor, is 7.7. From eq 4, an emission ratio factor of 57 is estimated, which is substantially higher than the experimental C value (6) that was derived from the intensity map (Figure 7B). To interpret such a discrepancy, we may consider that the signal trapped in the waveguide will lose part of its intensity due to scattering effects along the propagation in the film (being the scattered signal emitted by the surface), in a similar way that was performed in the estimation of the losses incurred by self-absorption in LSCs of liquid solutions of PbS QDs.[54] Considering a thin layer (as is the case for the **F6-Eu** film, in which a signal that is not trapped does not undergo any scattering process), we can rewrite the top surface optical conversion efficiency η_{sf} as

$$\eta_{sf} = \frac{1}{2}(1-R)\eta_{abs}\eta_f\eta_s[(1-\eta_t)+(1-\eta_{tr})] \qquad (6)$$

Inserting eqs 6 and 3 into eq 4, we obtain the effective emission ratio factor (C_{eff}):

$$C_{eff} = \left[\frac{2\eta_{tr}\eta_t}{(1-\eta_t)+(1-\eta_{tr})}\right]\frac{A_{sf}}{A_e} \qquad (7)$$

To attain an emission ratio factor of 6, the scattering factor in eq 7 (η_{tr}) is 0.40 (instead of 1, as initially considered), which yields an effective optical conversion efficiency of 1.7%.

3. CONCLUSIONS

In this work, the syntheses of two new urea-bipyridine-derived bridged organosilanes (**P5** and **P6**) have been achieved. Their hydrolysis−condensation under nucleophilic catalysis in the presence of Eu^{3+} salts led to luminescent bridged silsesquioxanes (**M5-Eu** and **M6-Eu**), which were compared with **M4-Eu**. The maximum value of incorporated Eu^{3+} in the materials strongly depends on the isomer used. A value of $11\%_w$ can even be reached without phase segregation for **M6′-Eu** as the 6,6′-isomer is strongly basic and is expected to form a cagelike complex involving urea and bipyridine fragments. Indeed, the photoluminescence of

these materials, particularly the energetic position of the $^5D_0 \rightarrow ^7F_0$ transition, evidence a significantly different complexation mode of the Eu^{3+} ions for **M6-Eu**, compared to **M4-Eu** and **M5-Eu**. Moreover, **M6-Eu** exhibits the highest absolute emission quantum yield value (0.18 ± 0.02) among these three materials. This value can also be increased (0.26 ± 0.03) upon the addition of a malonamide derivative that promotes light harvesting without modification of the emission and excitation spectra. In addition, **M6-Eu** can be processed as thin films by spin-coating on glass substrates, leading to plates that are covered by a thin layer (~54 nm) consisting of luminescent bridged silsesquioxanes exhibiting an emission quantum yield (0.34 ± 0.03) that is among the highest values reported for films of Eu^{3+}-containing hybrids and that may be used as luminescent solar concentrators (LSCs) with an optical conversion efficiency of ~4%. The emission ratio factor (C) was quantified through the mapping of the intensity of the red pixels, which allowed for a more consistent estimation for the transport losses, because of the scattering of the emitted light in the film and substrate (0.40), and then for the effective optical conversion efficiency (1.7%). This is a very rare example of the use of Ln^{3+}-containing hybrid thin film for LSCs. Moreover, the optical conversion efficiency of the **F6-Eu** films can be optimized increasing the Eu^{3+} concentration, the film thickness, and C, which opens the possibility of increasing the photocurrent generated by solar cells coupled to the **F6-Eu** LSC edges, relative to the same cells facing the sun.

■ ASSOCIATED CONTENT

ⓢ Supporting Information. Figure S1, Fourier transform infrared (FTIR) spectroscopy data; Figure S2, X-ray diffraction (XRD) patterns; Figures S3 and S11, optical micrographs; Figures S4−S6, S9, S13, and S14, emission spectra; Figures S7, S8, S10, and S15−S17, $^5D_0$ emission decay curves; Figure S12, excitation spectra; Figure S18, refractive index dispersion curve and experimental ellipsometric parameters; and Figure S19, SEM image. This information is available free of charge via the Internet at http://pubs.acs.org.

■ AUTHOR INFORMATION

Corresponding Author
*E-mail: lcarlos@ua.pt michel.wong-chi-man@enscm.fr.

■ ACKNOWLEDGMENT

■ REFERENCES

(1) Escribano, P.; Julián-López, B.; Planelles-Aragó, J.; Cordoncillo, E.; Viana, B.; Sanchez, C. *J. Mater. Chem.* **2008**, *18*, 23.

(2) Binnemans, K. *Chem. Rev.* **2009**, *109*, 4283.

(3) Carlos, L. D.; Ferreira, R. A. S.; de Zea Bermudez, V.; Ribeiro, S. J. L. *Adv. Mater.* **2009**, *21*, 509.

(4) Carlos, L. D.; Ferreira, R. A. S.; de Zea Bermudez, V.; Julián-López, B.; Escribano, P. *Chem. Soc. Rev.* **2011**, *40*, 536.

(5) Jin, T.; Inoue, S.; Machida, K.; Adachi, G. *J. Electrochem. Soc.* **1997**, *144*.

(6) Wang, H. Q.; Batentschuk, M.; Osvet, A.; Pinna, L.; Brabec, C. J. *Adv. Mater.* **2011**, *23*.

(7) Machida, K.; Li, H.; Ueda, D.; Inoue, S.; Adachi, G. *J. Lumin.* **2000**, *87−9*, 1257.

(8) Misra, V.; Mishra, H. *J. Chem. Phys.* **2008**, *128*, 244701.

(9) Moudam, O.; Rowan, B. C.; Alamiry, M.; Richardson, P.; Richards, B. S.; Jones, A. C.; Robertson, N. *Chem. Commun.* **2009**, 6649.

(10) Wilson, L. R.; Rowan, B. C.; Robertson, N.; Moudam, O.; Jones, A. C.; Richards, B. S. *Appl. Opt.* **2010**, *49*, 1651.

(11) Reisfeld, R. *Opt. Mater.* **2010**, *32*, 850.

(12) van Sark, W. G. J. H. M.; Barnham, K. W. J.; Slooff, L. H.; Chatten, A. J.; Buchtemann, A.; Meyer, A.; McCormack, S. J.; Koole, R.; Farrell, D. J.; Bose, R.; Bende, E. E.; Burgers, A. R.; Budel, T.; Quilitz, J.; Kennedy, M.; Meyer, T.; Donega, C. D. M.; Meijerink, A.; Vanmaekelbergh, D. *Opt. Express* **2008**, *16*, 21773.

(13) Dienel, T.; Bauer, C.; Dolamic, I.; Bruhwiler, D. *Sol. Energy* **2010**, *84*, 1366.

(14) Calzaferri, G. *Top. Catal.* **2010**, *53*, 130.

(15) Zhao, D.; Seo, S. J.; Bae, B. S. *Adv. Mater.* **2007**, *19*, 3473.

(16) Wang, Y.; Li, H. R.; Feng, Y.; Zhang, H. J.; Calzaferri, G.; Ren, T. Z. *Angew. Chem., Int. Ed.* **2010**, *49*, 1434.

(17) Dong, D. W.; Jiang, S. C.; Men, Y. F.; Ji, X. L.; Jiang, B. Z. *Adv. Mater.* **2000**, *12*, 646.

(18) Pecoraro, E.; Ferreira, R. A. S.; Molina, C.; Ribeiro, S. J. L.; Messsaddeq, Y.; Carlos, L. D. *J. Alloys Compd.* **2008**, *451*, 136.

(19) Chamas, Z. E.; Guo, X. M.; Canet, J. L.; Gautier, A.; Boyer, D.; Mahiou, R. *Dalton Trans.* **2010**, *39*, 7091.

(20) Lenaerts, P.; Storms, A.; Mullens, J.; D'Haen, J.; Gorller-Walrand, C.; Binnemans, K.; Driesen, K. *Chem. Mater.* **2005**, *17*, 5194.

(21) Li, Y. H.; Zhang, H. J.; Wang, S. B.; Meng, Q. G.; Li, H. R.; Chuai, X. H. *Thin Solid Films* **2001**, *385*, 205.

(22) Li, H. R.; Fu, L. S.; Lin, J.; Zhang, H. J. *Thin Solid Films* **2002**, *416*, 197.

(23) Yan, B.; Sui, Y. L.; Liu, J. L. *J. Alloys Compd.* **2009**, *476*, 826.

(24) He, H. S.; Dubey, M.; Sykes, A. G.; May, P. S. *Dalton Trans.* **2010**, *39*, 6466.

(25) Sui, Y. L.; Yan, B. *J. Photochem. Photobiol. A* **2006**, *182*, 1.

(26) Armelao, L.; Bottaro, G.; Quici, S.; Scalera, C.; Cavazzini, M.; Accorsi, G.; Bolognesi, M. *ChemPhysChem* **2010**, *11*, 2499.

(27) Oh, E. O.; Kim, Y. H.; Whang, C. M. *J. Electroceram.* **2006**, *17*, 335.

(28) Benyahya, S.; Monnier, F.; Taillefer, M.; Wong Chi Man, M.; Bied, C.; Ouazzani, F. *Adv. Synth. Catal.* **2008**, *350*, 2205.

(29) Li, H. R.; Lin, N. N.; Wang, Y. G.; Feng, Y.; Gan, Q. Y.; Zhang, H. J.; Dong, Q. L.; Chen, Y. H. *Eur. J. Inorg. Chem.* **2009**, 519.

(30) Feng, Y.; Li, H. R.; Gan, Q. Y.; Wang, Y. G.; Liu, B. Y.; Zhang, H. J. *J. Mater. Chem.* **2010**, *20*, 972.

(31) Nobre, S. S.; Ferreira, R. A. S.; Cattoën, X.; Benyahya, S.; Taillefer, M.; de Zea Bermudez, V.; Wong Chi Man, M.; Carlos, L. D. *Spectrosc. Lett.* **2010**, *43*, 321.

(32) Franville, A. C.; Zambon, D.; Mahiou, R.; Troin, Y. *Chem. Mater.* **2000**, *12*, 428.

(33) Caix-Cecillon, C.; Chardon-Noblat, S.; Déronzier, A.; Haukka, M.; Pakkanen, T. A.; Ziessel, R.; Zsoldos, D. *J. Electroanal. Chem.* **1999**, *466*, 187.

(34) Thibault, M. E.; Luska, K. L.; Schlaf, M. *Synthesis* **2007**, 791.

(35) Broudic, J. C.; Conocar, O.; Moreau, J. J. E.; Meyer, D.; Wong Chi Man, M. *J. Mater. Chem.* **1999**, *9*, 2283.

(36) Bourg, S.; Broudic, J. C.; Conocar, O.; Moreau, J. J. E.; Meyer, D.; Wong Chi Man, M. *Chem. Mater.* **2001**, *13*, 491.

(37) Janiak, C.; Deblon, S.; Wu, H. P.; Kolm, M. J.; Klüfers, P.; Piotrowski, H.; Mayer, P. *Eur. J. Inorg. Chem.* **1999**, 1507.

(38) Albrecht, M.; Janser, I.; Lützen, A.; Hapke, M.; Fröhlich, R.; Weis, P. *Chem. Eur. J.* **2005**, *11*, 5742.

(39) Fox, M. *Optical Properties of Solids*; Oxford University Press: New York, 2002.

(40) Fernandes, V. R.; Vicente, C. M. S.; Wada, N.; André, P. S.; Ferreira, R. A. S. *Opt. Express* **2010**, *18*.

(41) Nobre, S. S.; Brites, C. D. S.; Ferreira, R. A. S.; de Zea Bermudez, V.; Carcel, C.; Moreau, J. J. E.; Rocha, J.; Wong Chi Man, M.; Carlos, L. D. *J. Mater. Chem.* **2008**, *18*, 4172.

(42) Nobre, S. S.; Cattoën, X.; Ferreira, R. A. S.; Wong Chi Man, M.; Carlos, L. D. *Phys. Status Solidi−RRL.* **2010**, *4*, 55.

(43) Carlos, L. D.; Ferreira, R. A. S.; de Zea Bermudez, V.; Ribeiro, S. J. L. *Adv. Funct. Mater.* **2001**, *11*.

(44) Nobre, S. S.; Lima, P. P.; Mafra, L.; Ferreira, R. A. S.; Freire, R. O.; Fu, L. S.; Pischel, U.; de Zea Bermudez, V.; Malta, O. L.; Carlos, L. D. *J. Phys. Chem. C* **2007**, *111*, 3275.

(45) Carlos, L. D.; Ferreira, R. A. S.; de Zea Bermudez, V.; Molina, C.; Bueno, L. A.; Ribeiro, S. J. L. *Phys. Rev. B* **1999**, *60*, 10042.

(46) Carlos, L. D.; Malta, O. L.; Albuquerque, R. Q. *Chem. Phys. Lett.* **2005**, *416*, 238.

(47) Malta, O. L.; Batista, H. J.; Carlos, L. D. *Chem. Phys.* **2002**, *282*.

(48) Thuéry, P.; Nierlich, M.; Charbonnel, M. C.; Den Auwer, C.; Dognon, J. P. *Polyhedron* **1999**, *18*, 3599.

(49) Dong, D. W.; Yang, Y. S.; Jiang, B. Z. *Mater. Chem. Phys.* **2006**, *95*, 89.

(50) Wang, Y.; Wang, Y. G.; Cao, P. P.; Li, Y. N.; Li, H. R. *CrystEngComm* **2011**, *13*, 177.

(51) Wang, Y.; Wang, Y.; Gan, Q. *Sol−Gel Sci. Technol.* **2010**, *56*, 141.

(52) Azzam, R. M. A.; Bashara, N. M., *Ellipsometry and Polarized Light*; Elsevier North-Holland: Amsterdam, New York, 1977.

(53) Ramsey, D. A.; Ludema, K. C. *Rev. Sci. Instrum.* **1994**, *65*, 2874.

(54) Shcherbatyuk, G. V.; Inman, R. H.; Wang, C.; Winston, R.; Ghosh, S. *Appl. Phys. Lett.* **2010**, *96*.